Received: 10 May 2022 | Revised: 24 November 2022 | Accepted: 4 February 2023

DOI: 10.33012/navi.581

ORIGINAL ARTICLE

Real-Time Ionosphere Prediction Based on IGS Rapid Products Using Long Short-Term Memory Deep Learning

Jianping Chen | **Yang Gao**

Department of Geomatics Engineering, University of Calgary

Correspondence
Jianping Chen,
2500 University Dr. NW, Calgary, AB Canada T2N 1N4.
Email: jian.chen1@ucalgary.ca

Abstract

High-precision ionospheric corrections are essential for precise positioning using low-cost single-frequency GNSS receivers. Although Real-Time Global Ionosphere Maps (RT-GIMs) are available from the International GNSS Service (IGS), their ionospheric predictions continue to rely on networks of globally-distributed GNSS stations and real-time data links. In this paper, we develop a regional real-time ionospheric prediction model based on a long short-term memory (LSTM) deep learning method. Because the GIMs from the IGS are used as prediction bases, the requirement for real-time GNSS data-links is eliminated. A comparison of the ionospheric predictions generated over 24 hours by the proposed method and the IGS GIM revealed a prediction accuracy root mean square error of 0.8 TECU. These results suggest that the proposed model may be suitable for use in real-time applications.

Keywords

deep learning, Ionospheric prediction, LSTM, neural network

1 | INTRODUCTION

The ionosphere is the layer of the Earth's atmosphere at heights between 50 km to 1300 km that contains most of the free electrons (Perez, 2018). The ionospheric layer causes a group delay in code measurements and advances in carrier phase measurements. The GNSS error caused by the ionosphere is the most significant when compared to other errors. Precise ionospheric information and modeling will therefore be useful to mitigate its effects on single-frequency receiver users and improve the convergence time and performance of dual-frequency receivers (Aggrey & Bisnath, 2019; Liu et al., 2021).

The International GNSS Service (IGS) has developed the Global Ionosphere Map (GIM) in the IONosphere EXchange (IONEX) format (Schaer & Gurtner, 1998) with archived map data dating back to 1993. The typical spatial resolution of the GIMs is 2.5° in latitude and 5° in longitude, thus providing 71 x 73 grids globally (Schaer, 1997). Currently, there are three main types of IGS GIMs in terms of latencies, i.e., final, rapid, and predicted. The final GIM has an accuracy of 2–8 TECU and is thus a more accurate ionosphere map compared to the other two types (Products, 2020). Largely due to efforts and various approaches from

several IGS analysis centers, results from a recent analysis revealed improvements in the quality of predicted ionosphere measurements generated by most IGS processing centers which are now close to those of the post-processed GIMs (Liu et al., 2021). The IGS real-time service (RTS) generates real-time products including satellite orbits, clocks, code/phase biases, and RT-GIMs (Liu et al., 2021). The RT-GIM is described in the form of spherical harmonics with an order of 15 that saves broadcast bandwidth. This follows the RTCM-SSR (RTCM-SC, 2014) and IGS-SSR (IGS, 2020) formats. The RT-GIMs from the Centre National d'Études Spatiales (CNES) upgraded the spherical harmonic degree from 6 to 12 on June 22, 2017; at this time, the IGS RT-GIMs use a harmonic degree of 15 (Liu et al., 2021). The CNES quality assessment revealed that the use of a spherical harmonic degree of 12 resulted in a lower bias of up to 3 TECU while the use of a degree of 6 resulted in a higher bias of 5 TECU (Nie et al., 2019). Additional analysis demonstrated that the use of spherical harmonic degrees of 17 or 20 improved the precision by 3.19% and 6.06%, respectively, compared to the degree of 15 (Products, 2020). An annual comparison between CNES real-time products and IGS final GIMs revealed that the bias ranges from -4.36 to 0.86 TECU and root mean square (RMS) Es ranging from 0.8 to 7.04 TECU (Nie et al., 2019). Although the quality of the IGS rapid products has improved and they are now comparable with the IGS final products, the real-time broadcast ionosphere products that use spherical harmonic models still show considerable errors besides that of the original prediction products because they lose many details compared to rapid and final products. Additionally, the IGS prediction approaches require continuous GNSS data links which renders their services vulnerable to the reliability of the Internet infrastructure.

Because ionosphere prediction is a highly non-linear and complex task, several alternative methods based on neural network (NN) models have been introduced, including convolutional neural networks (CNNs) and recurrent neural networks (RNNs) (Ferreira et al., 2017; Habarulema et al., 2011; Leandro & Santos, 2007; Mallika et al., 2019; Mallika et al, 2020; McKinnell & Poole, 2004; Uwamahoro et al., 2018). NN models have been in existence for several decades and have been widely used in many applications, including meteorological prediction and share market forecasts, among others (Haykin, 2009; Karevan & Suykens, 2020). To improve their accuracy, researchers have applied different NN models for regional and global ionosphere prediction (Kaselimi et al, 2020; Leandro & Santos, 2007; McKinnell & Poole, 2004). For example, Ferreira et al. (2017) investigated several input parameter combinations and activation functions for regional ionosphere prediction. The results of their study revealed that the input parameter selection plays an important role in improving the accuracy of the NN model. Likewise, Kaselimi et al. (2020) attempted to use CNN to provide a receiver-side slant ionosphere prediction, while Hochreiter and Schmidhuber (1997) introduced Long-Short Term Memory (LSTM) units to address the gradient vanishing problem in the traditional RNNs. Following this, many researchers began to apply LSTM-based methods to ionosphere prediction. For example, Sun et al. (2017) compared the performance of total electron content (TEC) prediction using LSTM models. Their results revealed that LSTM outperformed the existing methods. Similarly, Tang et al. (2020) performed an additional analysis aimed at comparing the performance of autoregressive integrated moving average (ARIMA), LSTM, and seq2seq (sequence-to-sequence) methods during a geomagnetic storm; their results suggested that LSTM achieved the best performance. Liu et al. (2020) attempted to use LSTM to forecast 256 spherical harmonic coefficients; a two-hour ionospheric prediction was performed based on the forecasted parameters. Xiong et al. (2021) used information from 15 stations

to generate regional vertical total electron content (VTEC) over China and found that the Encoder-Decoder (ED)-LSTM outperforms the other three machine learning models. Ulukavak (2021) analyzed another regional ionosphere prediction using the LSTM-based deep learning method and found that the ionosphere prediction from the deep learning method was accurate enough to meet the requirements for communication and navigation applications. Lluire and Lu (2022) used Gated Recurrent Unit (GRU) and LSTM to predict the ionosphere at a station in Kenya. The results revealed GRU outperforms the other models, including LSTM. GRU is the newest entrant to this field after RNN and LSTM. It was introduced by Chung et al. (2014). Stations in Kenya were used to generate the local VTEC which was then used to train the model. Training and validation RMSE plots were used to determine the number of neurons required for the research. Generally, GRU and LSTM are better than other models. Also, GRU performs better than LSTM during intense geomagnetic events. Han et al. (2022) used VTEC data derived from three stations from 2012 to 2014 for training and data collected in 2015 for testing. The selected period exhibited the highest solar activity in the recent 12 years.

Four machine learning models, including NN, LSTM, adaptive neuro-fuzzy inference system (ANFIS), and gradient-boosted decision trees (GBDTs) were ana-lyzed for this research. Machine learning methods can achieve 2.9–4.7 TECU pre-diction accuracy during periods of high solar activity period; the GBDT approach results in a 5.6% improvement compared to other machine learning methods. Xia et al. (2021) investigated the performance of encoder-decoder convolution long short-term memory (ED-ConvLSTM) for medium-term ionosphere prediction on a global scale based on IGS GIMs. In 2018, this approach achieved 2.04 TECU for a five-day model. Although LSTM has performed effectively and has provided accu-rate ionosphere predictions, existing research has employed only a single LSTM layer. Therefore, it will be worthwhile to investigate the impact of the number of LSTM layers on prediction accuracy and validate the prediction using GNSS posi-tioning techniques.

In this paper, we propose an ionosphere prediction approach based on a sequence-to-sequence LSTM deep learning method that can accommodate short-term regional ionosphere predictions to achieve improved prediction accu-racy. The proposed model uses multiple LSTM layers to capture both long-term and short-term ionosphere VTEC variations. The proposed model has been applied to predict regional ionosphere delays over a northwestern region of North America based on precise rapid products from IGS with one to two days latency. Rapid prod-ucts from the Center for Orbit Determination in Europe (CODE) generated over a period of 90 days were used to train the model. The evaluation of the prediction performance includes a comparison of the pseudorange-based positioning infor-mation derived from the proposed ionosphere model with the original rapid prod-ucts from CODE.

The main goal of this research is to improve the quality of rapid products so that they can be used in real-time applications without a significant loss of accuracy. The rapid products have at least one day of latency and the existing real-time spher-ical harmonics products have up to 5 TECU of degradation. This research suggests the possibility of using the precise ionosphere from the rapid products in real-time by applying a two-LSTM-layer deep learning method with continuous daily updat-ing of newly-available rapid products.

The paper is arranged as follows. The methodology of the LSTM deep learning method and the associated evaluation methods are discussed first. The next section includes test cases and results followed by an analysis of the performance of the ion-osphere. The paper ends with a set of conclusions and a discussion of future work.

2 | METHODOLOGY

The feed-forward (FF) NN is a straightforward model that includes one or more fully connected dense layers. The hidden layers contain neurons that simulate pathways in the human brain. Traditional NNs are effective at finding and mapping complex nonlinear relationships between sets of inputs and outputs. The training process uses a known set of inputs and outputs that adjusts and eventually identifies a set of converged weights and biases associated with these neurons. The goal of the adjustment procedure is to minimize the differences between the NN output and the true output from the training dataset. Because the relationship between inputs and outputs is typically complicated and nonlinear, the adjustment needs to undergo multiple iterations to reach convergence. The converged weights and biases generate the best-fit model for the training inputs and outputs. The model then can be used to predict unknown outputs based on a new set of inputs. In this research, a fully-connected FFNN was first used to predict sequences of the ionosphere. The seasonal and diurnal parameters included in the input list are represented by the quadrature components, including the day of the year (DoY) and hour of the day (HoD). These components are described in Equations (1) and (2) as follows (McKinnel and Poole, 2004):

$$HC = \cos\left(\frac{2\pi \times t}{24}\right), HS = \sin\left(\frac{2\pi \times t}{24}\right) \tag{1}$$

$$DNC = \cos\left(\frac{2\pi \times d}{365.25}\right), DNS = \sin\left(\frac{2\pi \times d}{365.25}\right) \tag{2}$$

The other inputs of the FFNN are latitude, longitude, and Kp-index. A two-layer setting is used with each hidden layer containing 10 neurons. Of note, the use of too many neurons can lead to problems associated with overfitting. To overcome this problem, 80% of the data was selected at random and used to train the model; the remaining 20% was used to perform the validation. The Levenberg-Marquardt algorithm was used to train the model. Figure 1 documents the schematic structure used in the research.

FFNNs are clearly unsuitable for sequence prediction as they typically do not have a feedback loop needed to support online learning. By contrast, an RNN can incorporate new information via its internal loops. The loops allow the temporal information to be transferred between time frames. An easily-understood

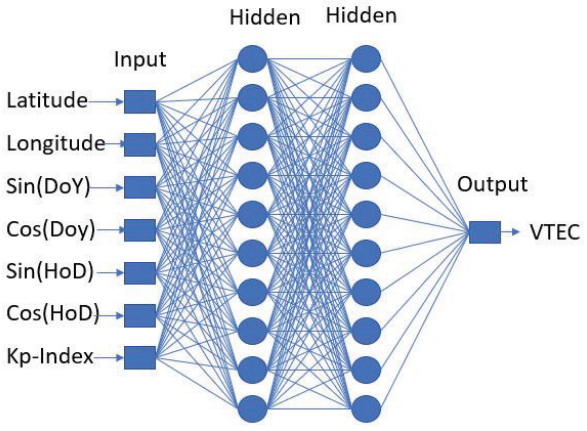

FIGURE 1 Architecture of the FFNN

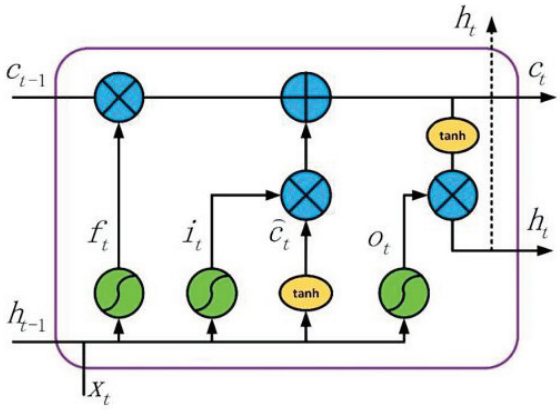

FIGURE 2 LSTM architecture (Fang, et al., 2020)

chain-like NN can be diagramed by "unrolling" an RNN cell. The LSTM network is a special form of RNN that can have the capacity to learn long-term dependency (Fang et al., 2020). Figure 2 shows the structure of a single LSTM block. The LSTM block has three gates, including the input gate i_t, forget gate f_t, and output gate o_t. Given the availability of a forget gate, an LSTM cell can add or subtract information regarding internal cell states.

Based on the data flow in the architecture, the mathematical model of LSTM can be summarized as described by Fang, et al. (2020) and shown in Equations (3)–(8).

$$f_t = \sigma(W_f[h_{t-1}, x_t] + b_f) \tag{3}$$

$$i_t = \sigma(W_i[h_{t-1}, x_t] + b_i) \tag{4}$$

$$\hat{c}_t = tanh(W_c[h_{t-1}, x_t] + b_c) \tag{5}$$

$$c_t = f_t^o \, c_{t-1} + i_t^o \, \hat{c}_f \tag{6}$$

$$o_t = \sigma(W_o[h_{t-1}, x_t] + b_o) \tag{7}$$

$$h_t = o_t^o \, tanh(c_t) \tag{8}$$

In this research, LSTM was selected as the prediction model. A typical LSTM NN contains one sequence input layer that prepares the data for the following LSTM layers. This type of NN also has one or more LSTM layers, including one fully-connected dense layer and one output layer. The proposed NN is illustrated in Figures 3 and 4 for training and prediction processes. Here, MAP represents ionosphere grid map. As shown, the original training dataset was used as input and the same dataset with a one-hour shift was used as output. Given the known inputs and outputs, the goal of the training process is to find the best fit for the internal parameters. By contrast, the prediction process uses one map as input. The output will be the predicted map one hour into the future. The prediction algorithm persists until new daily ionosphere maps, which are provided by new updated rapid product files in IONEX format, are available. The new file is updated by additional tuning of the model so that the

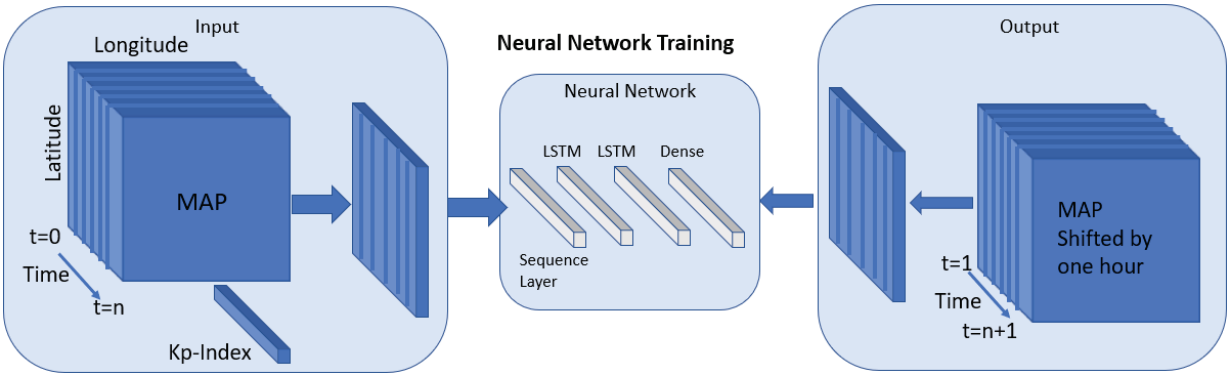

FIGURE 3 Temporal deep learning LSTM NN architecture for training

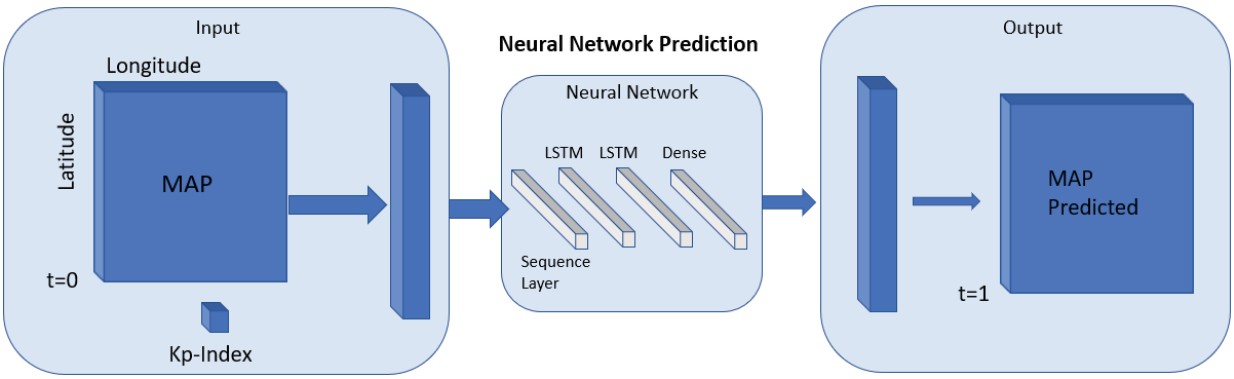

FIGURE 4 Temporal deep learning LSTM NN architecture for prediction

maximum prediction file will be generated within one day, given that the rapid product update rate is 24 hours. The sequence layer can handle time dimensions of different sizes. The output from the sequence layer will be always equal to the so-called number of features which is equal to the flattened one-hour ionosphere map.

The number of hidden units in the LSTM layer is determined by a trial-and-error process. The use of too few units will lead to underfitting while the use of too many units will result in overfitting. To find the best-fit number of units to be used in this research, a variety of sets of numbers were evaluated. Using the October 9 dataset as an example, we divided the dataset into two groups, including one training dataset, and one test dataset; 90% of the data was used to train the LSTM model and the remaining 10% was used to check the model accuracy. We evaluated 100, 200, 300, 400, and 500 LSTM units using the same dataset. The histogram plots representing our findings are shown in Figure 5. This analysis indicated that 400 units were the best setting for our dataset; 120 events were below 0.4 TECU.

The following analysis is based on the use of the same 400 LSTM units in the first layer. The same testing was performed for the second layer. Testing with 100, 200, 300, and 400 hidden units resulted in average test RMSEs of 0.59, 0.60, 0.62, and 0.59 TECU, respectively. Because the difference between 100 to 400 units is minimal, we arbitrarily selected half of the number of the first layer ($n = 200$ units), because the use of fewer units typically results in a more rapid training process. With 400 and 200 units used for the first and second layers, respectively, the total training time for the 90-day dataset was approximately one hour using a Dell laptop.

The original NN input contained three-dimensional data for time (hourly), latitude, and longitude and an optional one-dimensional Kp-index (three-hour

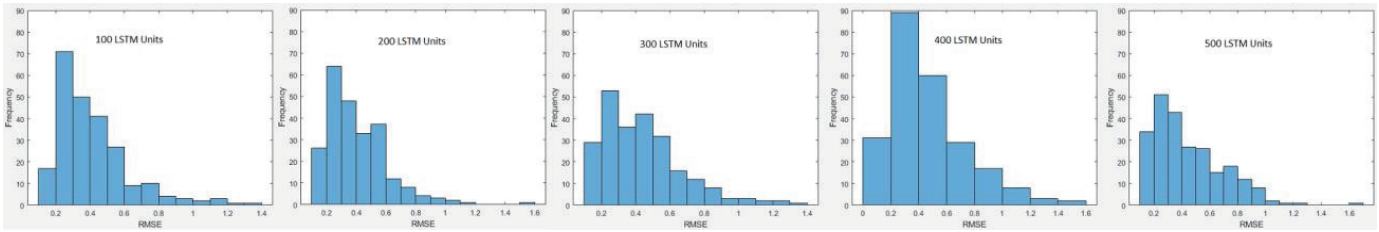

FIGURE 5 Test RMSE with different LSTM units

TABLE 1
Parameters of the LSTM Model

Parameters	Value
Activation Function	Relu
Max Epochs	250
Number of LSTM Layers	2 or 1
1st LSTM Layer Hidden Units	400
2nd LSTM Layer Hidden Units	200
3rd LSTM Layer Hidden Units	200
Number of Dense Layers	1
Learning Rate	0.005
Optimizer	Adam
Dropout	0.2
Loss function	MSE

interval). The one epoch map data is six grids (latitude) by 8 grids (longitude) or a total of 48 grid points. In the time domain, the training data covers 2160 epochs. Thus, the dimension of the training map data is 2160 x 6 x 8. The Kp-index data has a three-hour interval, which is lower than the ionosphere map time interval; thus, the previous value for the middle two hours is maintained. The training data were then flattened to two-dimensional input that included time, a one-dimensional ionosphere, and Kp-index values as needed. Thus, the NN contains one sequence layer, one LSTM layer with 400 hidden units, and two optional LSTM layers each with 200 hidden units, followed by a fully-connected dense layer. The fully-connected dense layer provides flexibility to the chosen number of the stacked LSTM hidden units as it transfers the number of hidden units to the number of features. The dense layer has the same dimension as the flattened training ionosphere map. The output of a one-dimensional map is then restored to a two-dimensional map for further analysis. Table 1 presents the parameters of the LSTM used in these experiments.

Figure 6 presents a flowchart of the proposed real-time ionosphere services. The entire system consists of two major parallel-running model-training and model-predicting threads. The former thread was used to train and update the LSTM model, and the latter thread was used for real-time ionosphere predictions. At the initialization stage, the 90-day rapid products are used in the initial training phase. During the days to follow, the thread checks periodically for new daily rapid products. Whenever a new map becomes available, it will be introduced and used to update the LSTM model. This means that the new maps will be used to tune an already-trained model so that only one-day prediction information will be needed going forward. At this point, the updated model, technically speaking, has been trained by the initial 90-day data together with data from various days

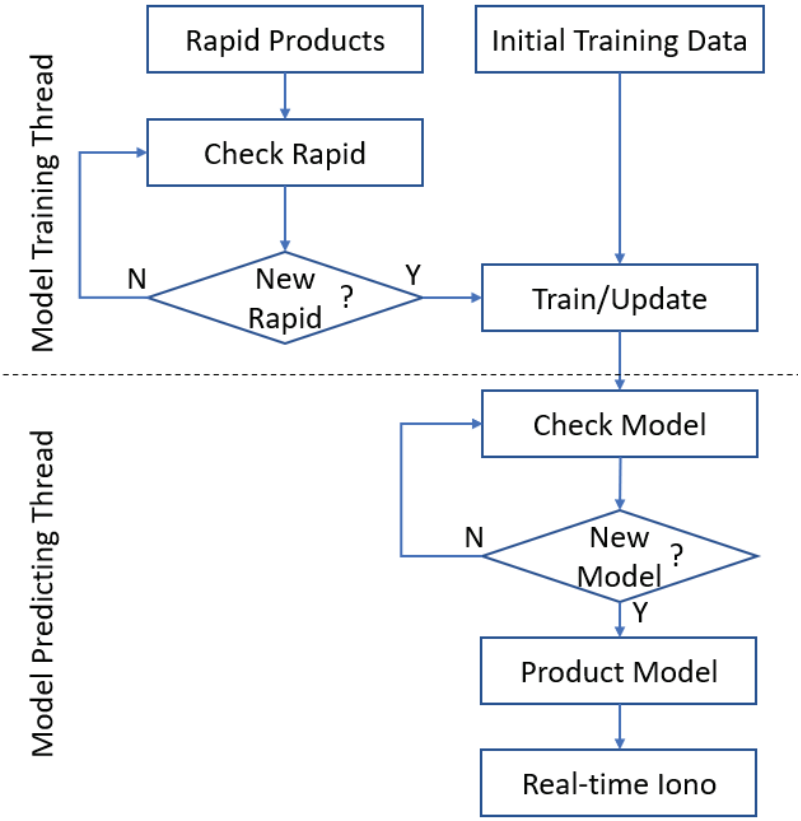

FIGURE 6 Flowchart of data processing

that have been used to update the model. The trained model thus has an update interval of one day. With respect to ionosphere prediction, the thread checks the newly-updated trained model and tries to use the most recent model to generate a prediction. In other words, the prediction thread attempts to reduce the prediction time to as small an interval as possible. The end-user could then use the pre-generated IONEX from the LSTM model as the real-time product. An alternative real-time application might include methods to generate ionosphere products directly from the trained model.

3 | EXPERIMENTS AND RESULTS

3.1 | Test Datasets

To test the ionosphere predictions with different geomagnetic activity strengths, two different target date ranges were selected: May 12–18 and October 9–15, 2021. On these dates, the daily peak Kp-indices were 7 and 2, respectively. Figure 7 shows the Kp index plots from National Oceanic and Atmospheric Administration / Space Weather Prediction Center (NOAA/SWPC).

A single region in the northwest of North America was selected as a target. The target region includes the entire northwest of the continental U. S. and the western region of Canada, with longitude ranging from 95° to 130° west, and latitude ranging from 40° to 52.5° north. The ionosphere grid resolution is the same as that of the IGS GIM, which is 5° longitude by 2.5° latitude and provides 48 (eight by six) grid points per map epoch. Figure 8 shows the region selected for the experiment.

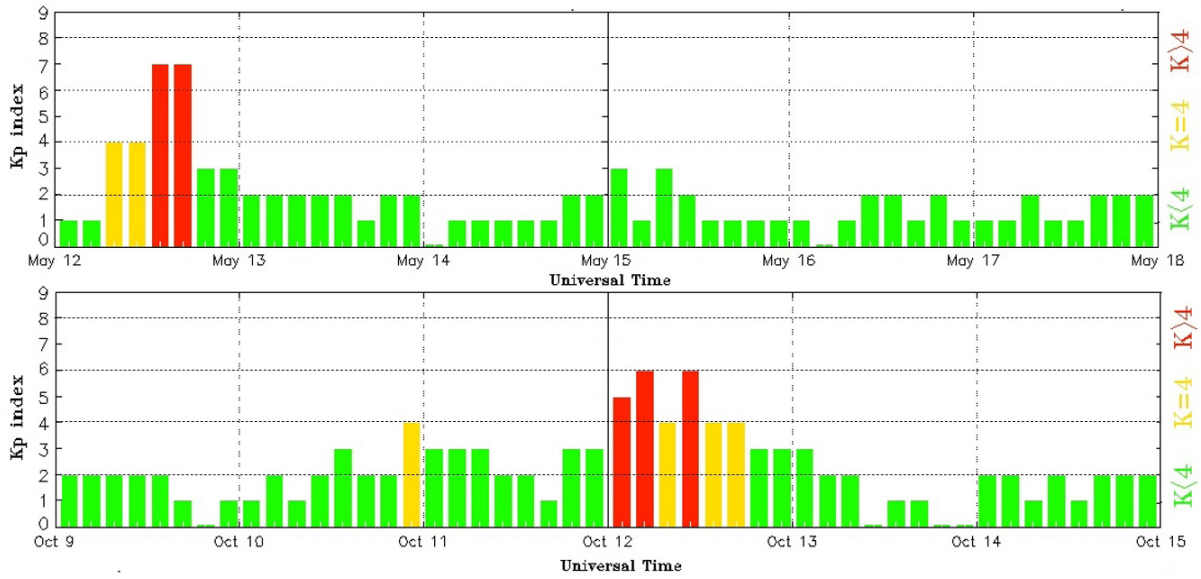

FIGURE 7 Kp-indices on May 12-18 and October 9-15

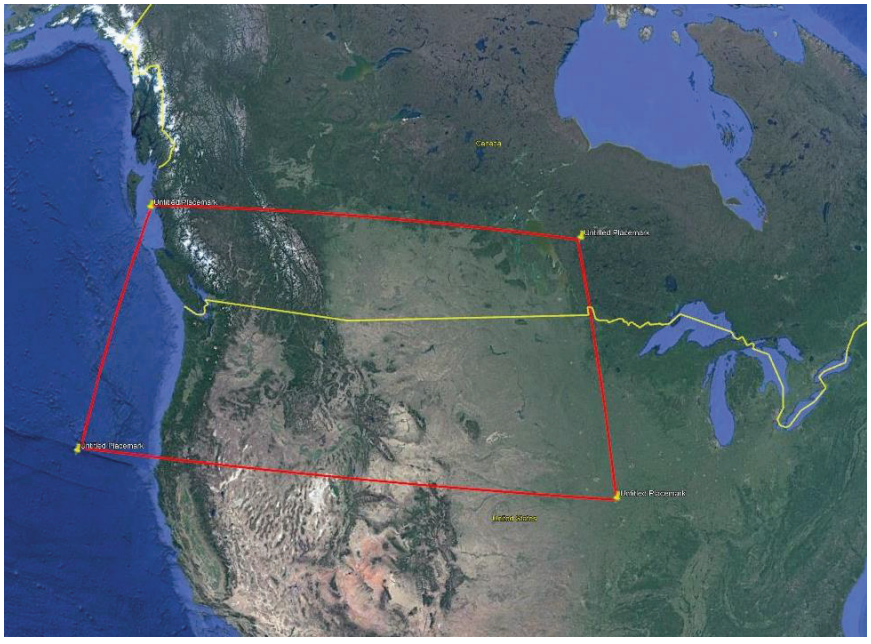

FIGURE 8 The regional coverage

The rapid products from CODE with the prefix "corg" were used in this analysis. The first time-window was between February 11 to May 12, 2021; the second was between July 11 and October 9, 2021. Kp-index data from the same time-windows as the ionosphere data were retrieved from NOAA/SWPC FTP site (ftp.swpc.noaa.gov). A total of four datasets were used; specific details are listed in Table 2. Datasets 1 and 2 are from July to October 2021; datasets 3 and 4 are from February to May 2021. Datasets 1 and 3 do not include Kp-indices; datasets 2 and 4 do include Kp-indices.

Because each time window includes 90 days while the corg products are hourly maps, the data dimensions for datasets 1 and 3 are 2160 (time) x 8 (longitude) x 6 (latitude) without the Kp-index. The two-dimensional maps are then flattened to

TABLE 2
Dataset Details

Dataset	Area Longitude	Area Latitude	Start Time	End Time	With Kp-index
1	-130° ~ -95°	40° ~ 52.5°	Jul 11, 2021	Oct 9, 2021	No
2	-130° ~ -95°	40° ~ 52.5°	Jul 11, 2021	Oct 9, 2021	Yes
3	-130° ~ -95°	40° ~ 52.5°	Feb 11, 2021	May 12, 2021	No
4	-130° ~ -95°	40° ~ 52.5°	Feb 11, 2021	May 12, 2021	Yes

TABLE 3
Test Case Description

Case	Dataset	Input Dimension	Neural Network
1	1	2160 * 48	48–400–48
2	1	2160 * 48	48–400–200–48
3	2	2160 * 49	49–400–49
4	2	2160 * 49	49–400–200–49
5	3	2160 * 48	48–400–48
6	3	2160 * 48	48–400–200–48
7	4	2160 * 49	49–400–49
8	4	2160 * 49	49–400–200–49
9	1	2160 * 48	48–400–200–200–48
10	2	2160 * 49	49–400–200–200–49
11	3	2160 * 48	48–400–200–200–48
12	4	2160 * 49	49–400–200–200–49

one dimension; thus, the final data dimensions for datasets 1 and 3 are 2160 x 48. For datasets 2 and 4 (with the Kp-index), the dimensions are changed to 2160 x 49.

As there are four kinds of datasets and three types of NN settings, including one model with one LSTM layer, one with two LSTM layers, and one with three LSTM layers, the experiment will include a total of 12 test cases as indicated in Table 3.

The input dimension was the time-axis by the number of features. For feature sets that do not include the Kp-index, this number is 48, and the cropped map is a 6 x 8 grid. For feature sets that do include the Kp-index, this information is appended as a final value. For the NN, the first number of neurons of the sequence layer equals the number of input features and the final number equals the output map dimensions. The middle numbers represent the hidden units of the LSTM layers.

3.2 | Accuracy of Ionospheric Prediction

In this section, we consider both hourly errors and daily errors. The maximum absolute error (MAXAE), the mean absolute error (MAE), and the root-mean-square error (RMSE) were all analyzed on an hourly and daily basis. The absolute error is given in Equation (9) as:

$$|\epsilon| = |VTEC_e - VTEC_r| \tag{9}$$

where ϵ is the error between the estimate and known ionosphere values, $VTEC_e$ is the estimated ionosphere, and $VTEC_f$ is the reference ionosphere. Thus, values for MAXAE, MAE, and RMSE can be calculated as shown in Equations (10)–(12):

$$\mathrm{MAXAE} = \max_{i=i:n}(\epsilon_i) \tag{10}$$

$$MAE = \frac{\sum_{i=1}^{n}|\epsilon_i|}{n} \tag{11}$$

$$RMSE = \sqrt{\frac{\sum_{i=1}^{n}(\epsilon_i)^2}{n}} \tag{12}$$

where the subscript i indicates each grid point and n is the total number of grids considered. For hourly statistics, the number is 48 (48 grids x 1 hour), and for daily statistics, this number should be 1152 (48 grids x 24 hours).

All four types of data were sent to the three types of predefined NNs, resulting in a total of 12 test cases. Table 4 documents the statistical results from all 12 test cases for the 24-hour prediction time.

As shown in Table 4, the test cases 1–4, 9, and 10 are from the lower Kp-index time-window datasets and 5–8, 10, and 11 are from the higher Kp-index time-window. Understandably, a lower Kp-index period will provide superior prediction performance. Also, we found that including an additional Kp-index as an extra feature (test cases 3, 4, 7, 8, 10, and 12) does not result in improved short-term predictions. This may be because the training period is relatively short compared to the solar activity period, which is 11 years. This also may be because the three-hour time resolution of the Kp-index data is somewhat too coarse for ionosphere prediction. Our findings also revealed that a single LSTM layer does not perform as well as two LSTM layers; however, adding additional LSTM layers after the first two also provided no better accuracy. The best cases are those that feature deep learning LSTM settings with a 400-LSTM-unit layer and a 200-LSTM-unit layer. With this design, the RMSEs for quiet and active periods are 0.79 and 1.66, respectively.

The findings shown in Figure 9 document the hourly statistical data for two datasets with one-layer and two-layer settings. On a day when the ionosphere was quiet (for example, October 9, 2021), although the results from a two-layer design are slightly better than one-layer, the overall difference is minimal.

TABLE 4
Test Results

Test Case	Neural Network	MAXAE (TECU)	MAE (TECU)	RMSE (TECU)
1	48–400–48	2.90	0.74	0.96
2	48–400–200–48	3.01	0.60	0.79
3	49–400–49	3.64	0.93	1.22
4	49–400–200–49	3.66	1.03	1.30
5	48–400–48	5.32	1.27	1.84
6	48–400–200–48	5.40	1.30	1.66
7	49–400–49	5.99	1.32	1.66
8	49–400–200–49	7.10	1.77	2.20
9	48–400–200–200–48	4.37	0.78	1.17
10	49–400–200–200–49	6.88	1.36	2.12
11	48–400–200–200–48	5.16	1.97	2.37
12	49–400–200–200–49	6.44	1.43	1.85

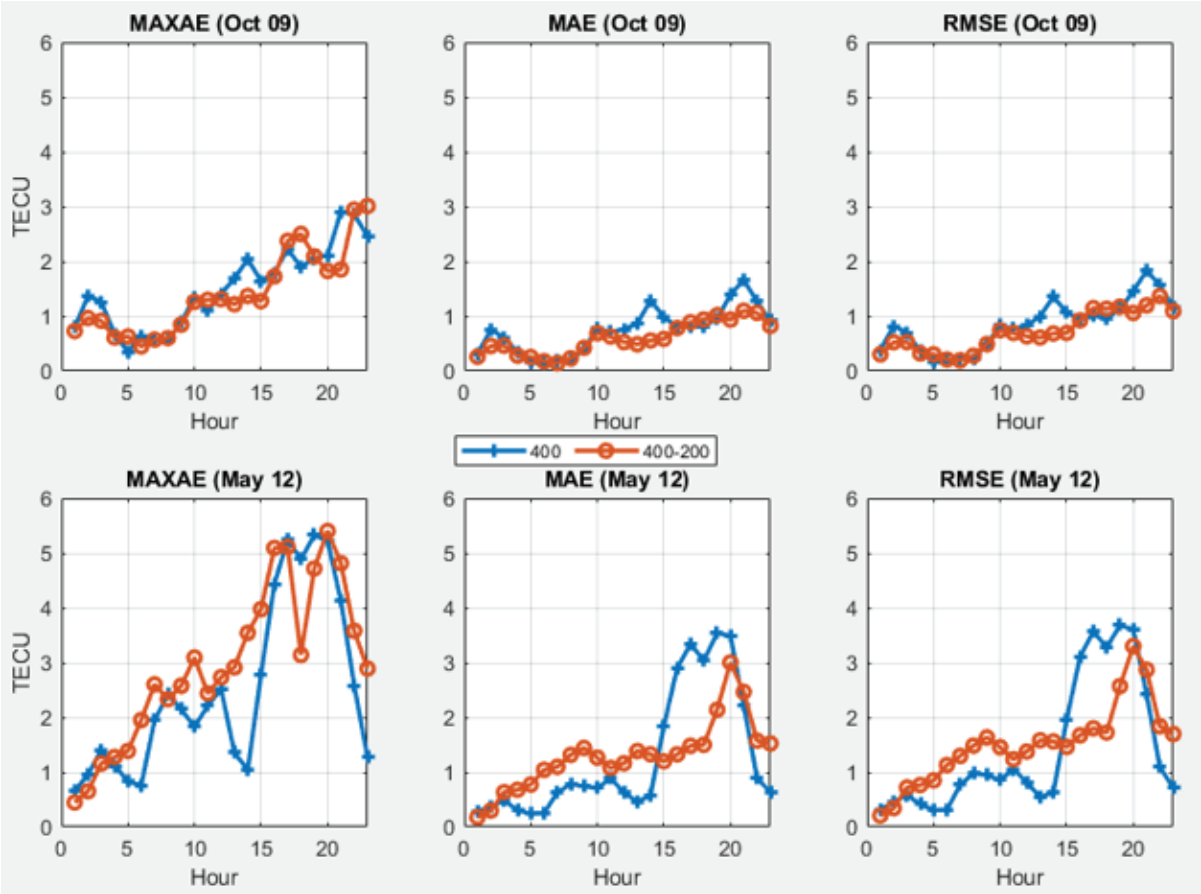

FIGURE 9 Hourly MAXAE, MAE, and RMSE for October 9 and May 12, 2021: ionosphere prediction

By contrast, on an active day (for example, May 12, 2021), the two-layer model shows greater stability over a longer prediction time, while performing similarly for a shorter prediction time. The two-LSTM-layer deep learning setting is clearly better in terms of stability and accuracy. Based on the 48–400–200–48 setting, Figure 10 documents the prediction performance of a typical geomagnetically quiet day with a sampling time of 12 hours. These results indicate that the south-easternmost part of UTC 23 and the north-westernmost part of UTC17 can achieve -3 and 2 TECU, respectively. Most of the day, the absolute errors are within ±1 TECU. Figure 11 documents the high ionosphere activity on May 12, 2021. Our findings indicate that a prediction accuracy at ±2 TECU can be achieved under most circumstances, even when the ionosphere activity is high.

We observed only insignificant prediction accuracy (Figures 10 and 11); thus, the predicted ionosphere products can be used for real-time applications. Because the rapid products have at least one day of latency, while the proposed prediction does not, the use of this method can improve the accuracy of rapid products close to those of real-time measurements. The predicted products can be in the form of IONEX files or generated directly by the trained NN model.

Results from an IGS broadcasting ionosphere stream (IONO00IGS1) in the form of spherical harmonics as shown. Figure 12 documents the comparison between IGS real-time and IONEX from CODE for 12 hours on Oct 9, 2021; Figure 13 documents the same comparison on May 12, 2021. A comparison of the predicted with the broadcast ionosphere revealed that the daily RMSE from October 9 improved

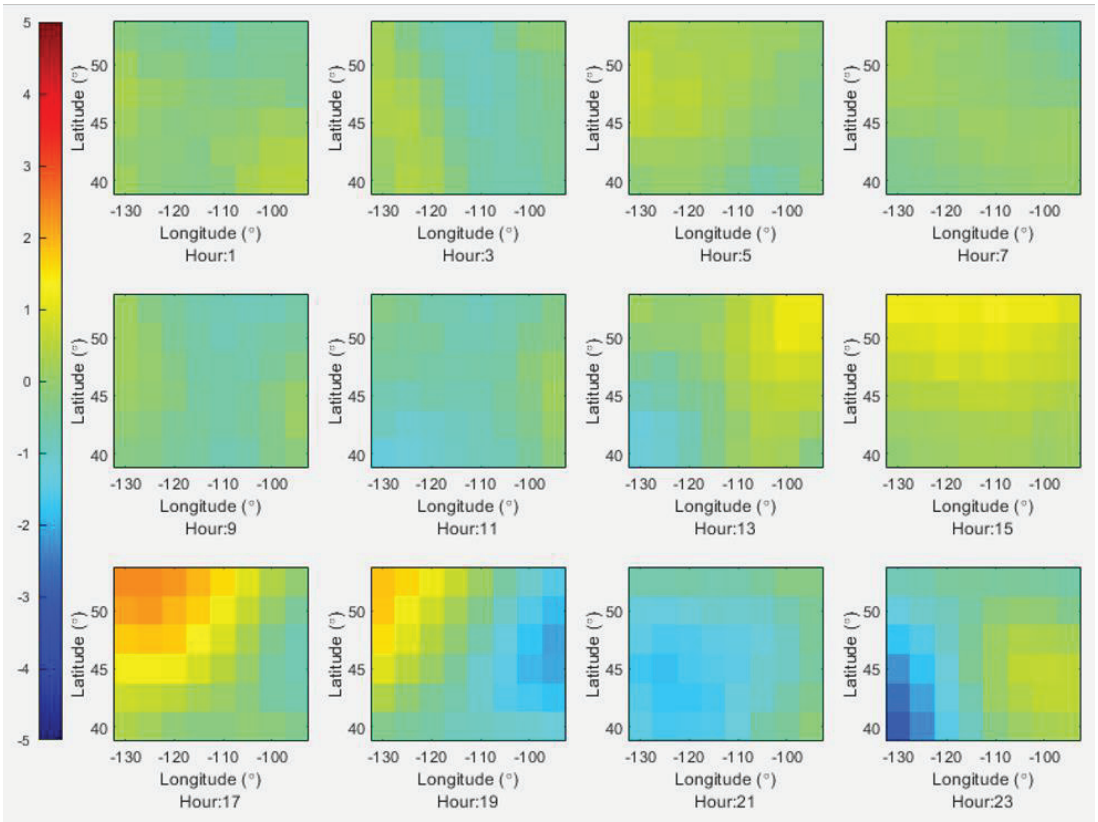

FIGURE 10 October 9, 2021: prediction error plots

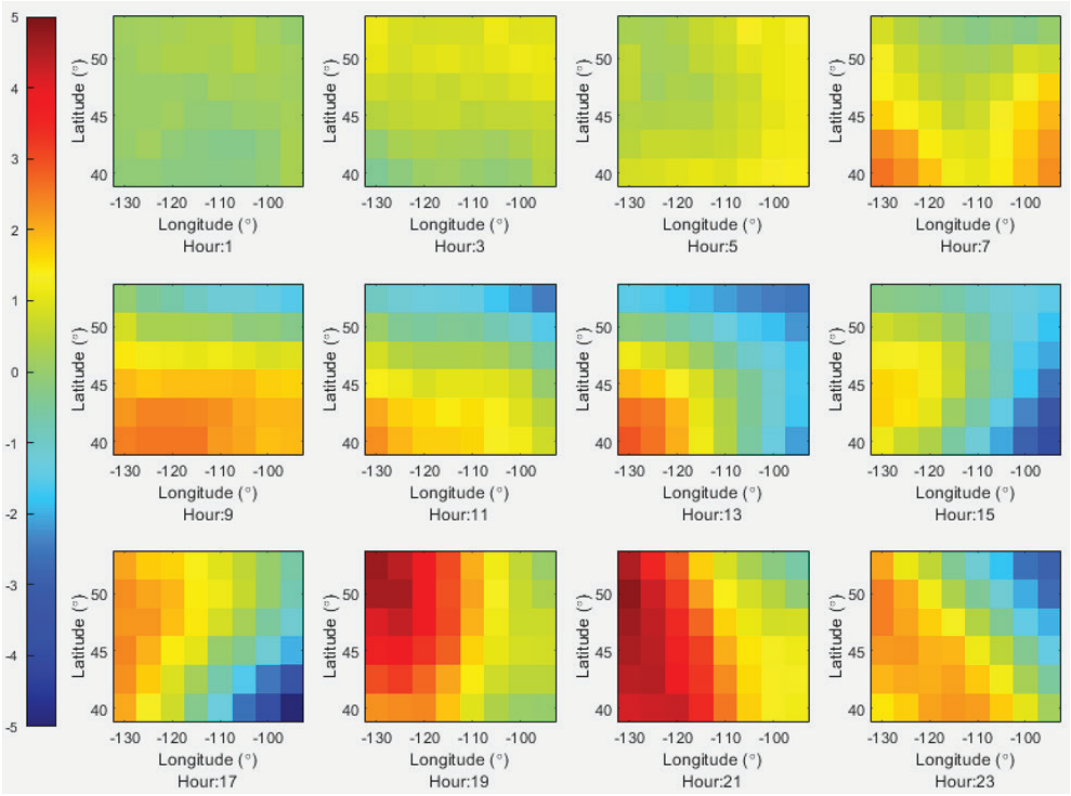

FIGURE 11 May 12, 2021: prediction error plots

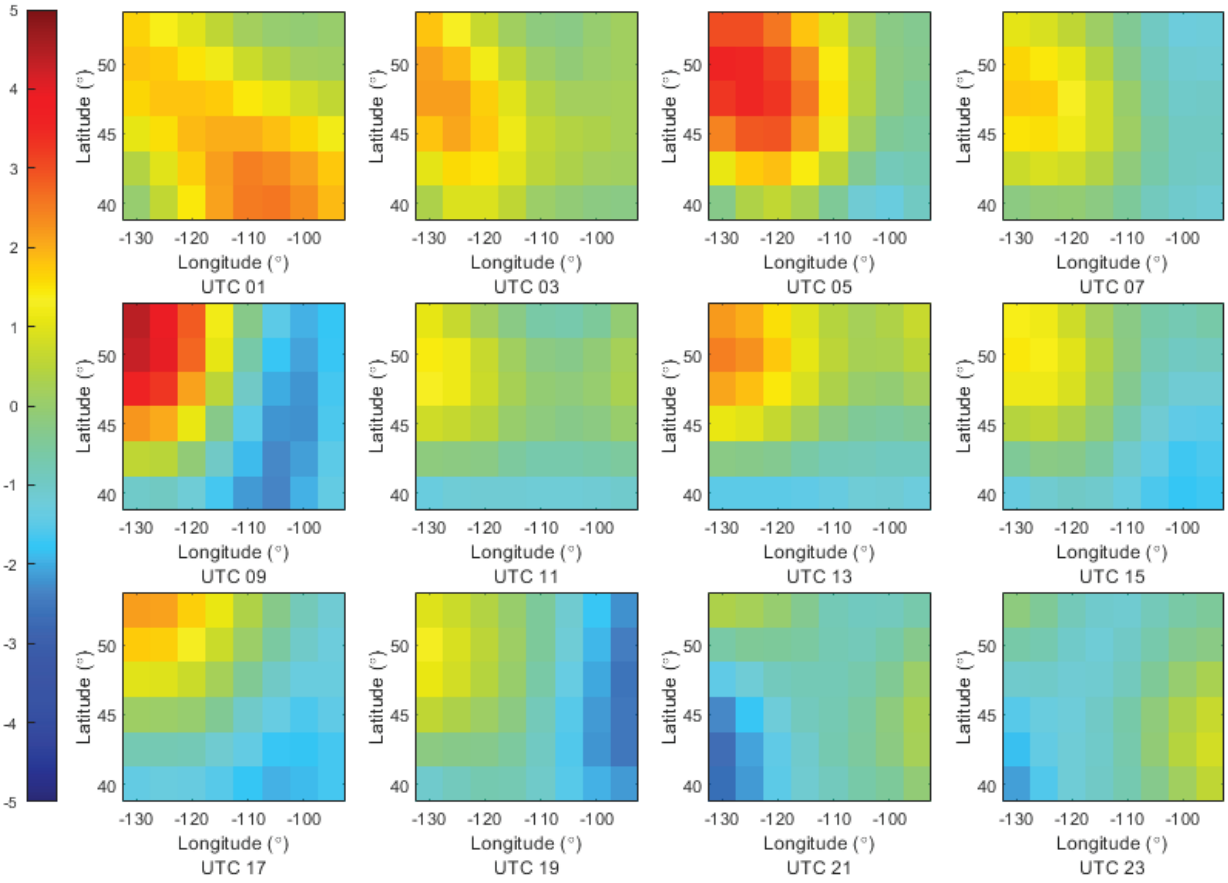

FIGURE 12 October 9, 2021: comparison between the broadcasting ionosphere and CODE rapid products

from 1.25 TECU to 0.79 TECU and that the daily RMSE from May 12 improved from 1.88 TECU to 1.66 TECU. These results indicate that the proposed ionosphere prediction outperforms the broadcast IGS products on both days and in response to different geomagnetic activity strengths.

To assess the VTEC for the covered area, the NN predicted products for the two-layer model, the one-layer model, the original rapid products, and the IGS broadcast spherical harmonic model were plotted for three NGS stations, i.e., mtcu, rkd1, and ptaa. These stations are also used in the subsequent GNSS verification process. From Figure 14, we can tell that for most of the 24-hour prediction time, the NN model-generated ionosphere maps appear very close to the rapid products which are used as a reference point for this research. Of the two NN models, the two-layer model is somewhat better than the one-layer model because it is closer to our reference (Ionex); by contrast, the IGS broadcast spherical harmonic model has shown difficulties in identifying the variations of the other two models.

As a real-time ionosphere service, the trained model needs to be updated with the newly available rapid products. The model can be updated without the need for a re-training. Figure 15 documents the impact of updating the model with the newly-available daily ionosphere map. The model is trained by 90-day data before hour 0. For the first 24 hours, the lines demarcating no update and hourly updates were aligned. After the first 24 hours, because the daily ionosphere information was used to update the model, divergence began to appear. During the first one-week

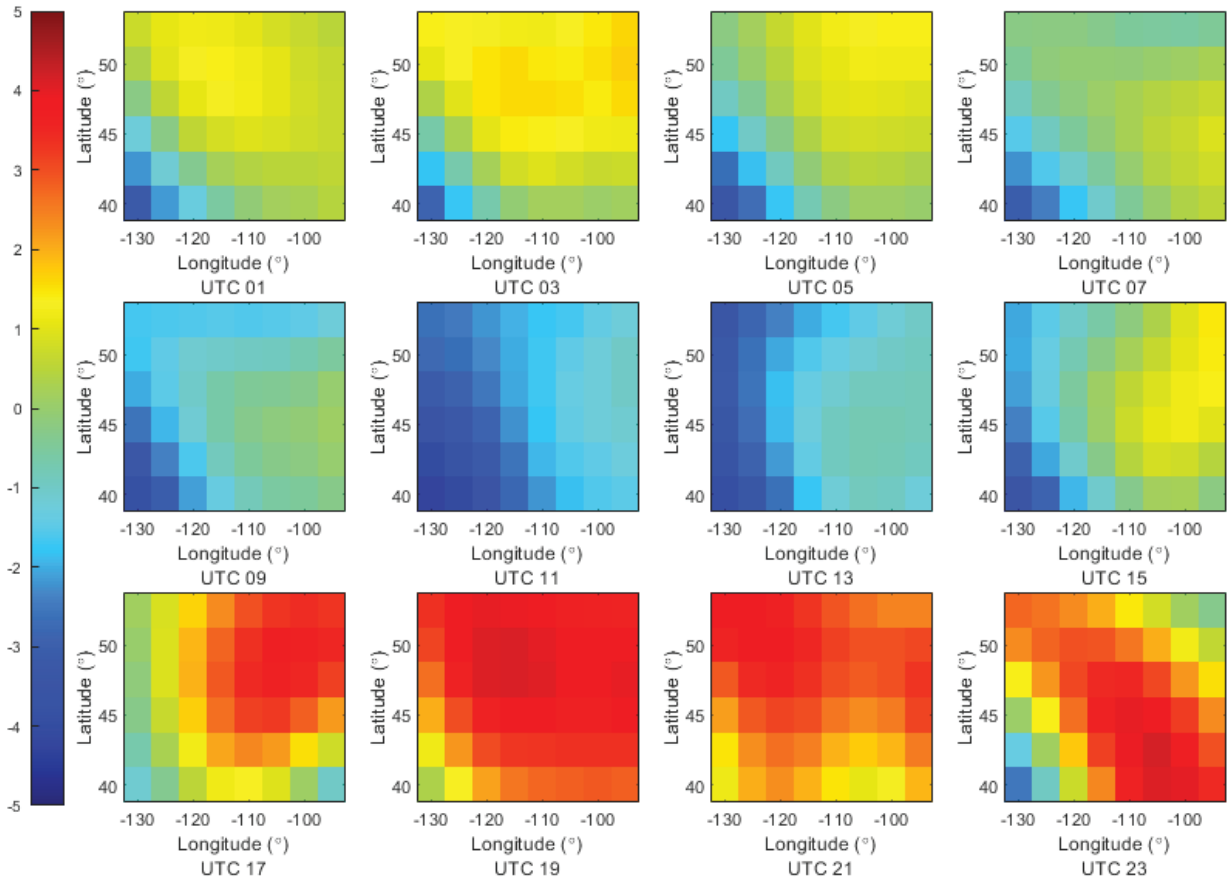

FIGURE 13 May 12, 2021: a comparison between the broadcasting ionosphere and CODE rapid products

period, the ionosphere is updated at 24, 48, 72, 96, 120, and 144 hours. The results show that, even with data outage persisting for as long as one week, the neural network model is capable of predicting the ionosphere map with reasonable accuracy, except UTC 18–20 of day 3 which underwent degradation up to 7.5 TECU RMSE. The use of a daily update model leads to significant reductions in RMSE. This was most notable on day 3, when the RMSE improved from up to 7.5 to values mostly below 1 TECU. Our result revealed that the daily updated model outperforms the long-time prediction model that has not undergone updating. As mentioned earlier, the real-time system has a detailed flow chart as described in Figure 6.

As we discussed above, the NN model is updated whenever there is a new daily rapid file is available. As a comparison, seven days of prediction are made with or without daily rapid product updates. The trained model that did not undergo daily rapid product updates was used to generate predictions for all seven days. By contrast, the one with daily rapid product updates uses true data to train the model by adding the additional true data information to the trained model. Figure 15 documents the performance of this method for seven days starting from May 12 and seven days starting from Oct 9, 2021. The results of our experiments reveal that daily updates demonstrate improved performance with better training with the latest rapid products. This is most apparent for the ionosphere active days. Table 5 shows the daily average RMSE for the seven days in May and seven days in October with daily rapid product updating.

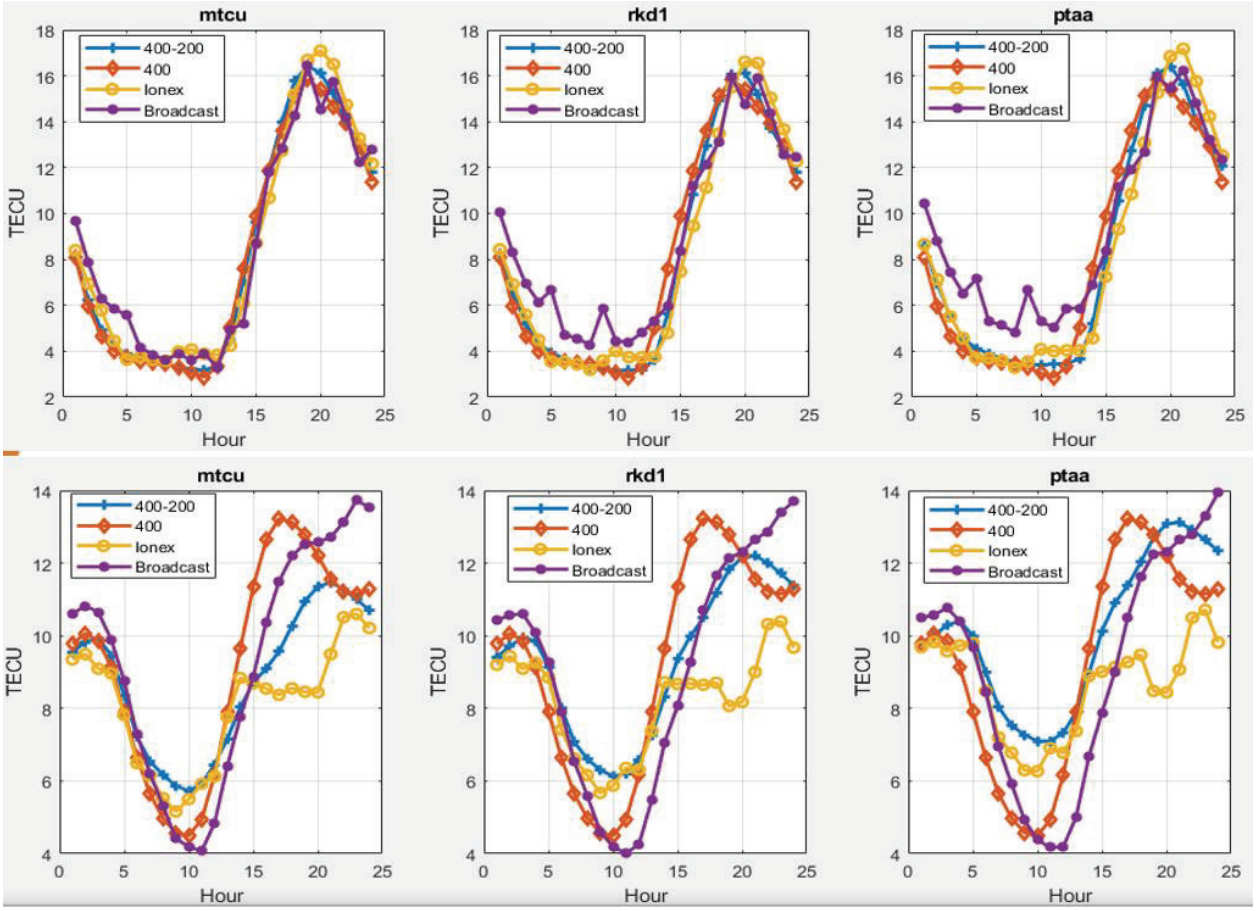

FIGURE 14 Three-Station (mtcu, rkd1, and ptaa) VTEC comparison of model prediction, rapid IONEX, and IGS broadcast spherical harmonics for the October 9 and May 12 datasets

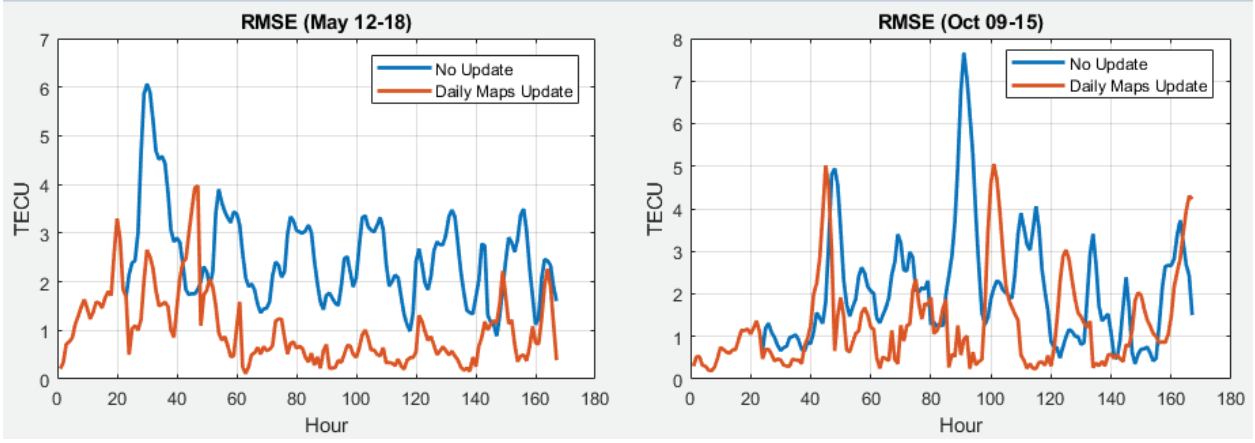

FIGURE 15 One-week prediction comparisons: with and without daily updates

To assess the performance of a fully-connected FFNN and the proposed LSTM real-time model, the predicted models are analyzed in the three evaluation stations described above. The original rapid products are also shown in comparison plots. Predictions from one-week intervals (May 12–18 and October 9–15) were used to document these differences. The plots show that the proposed LSTM

TABLE 5
One Week Prediction RMSE

Dates	RMSE (TECU)	Dates	RMSE (TECU)
May 12	1.66	Oct 9	0.79
May 13	1.96	Oct 10	1.37
May 14	1.21	Oct 11	1.22
May 15	0.63	Oct 12	1.20
May 16	0.53	Oct 13	1.76
May 17	0.57	Oct 14	1.18
May 18	0.92	Oct 15	1.42

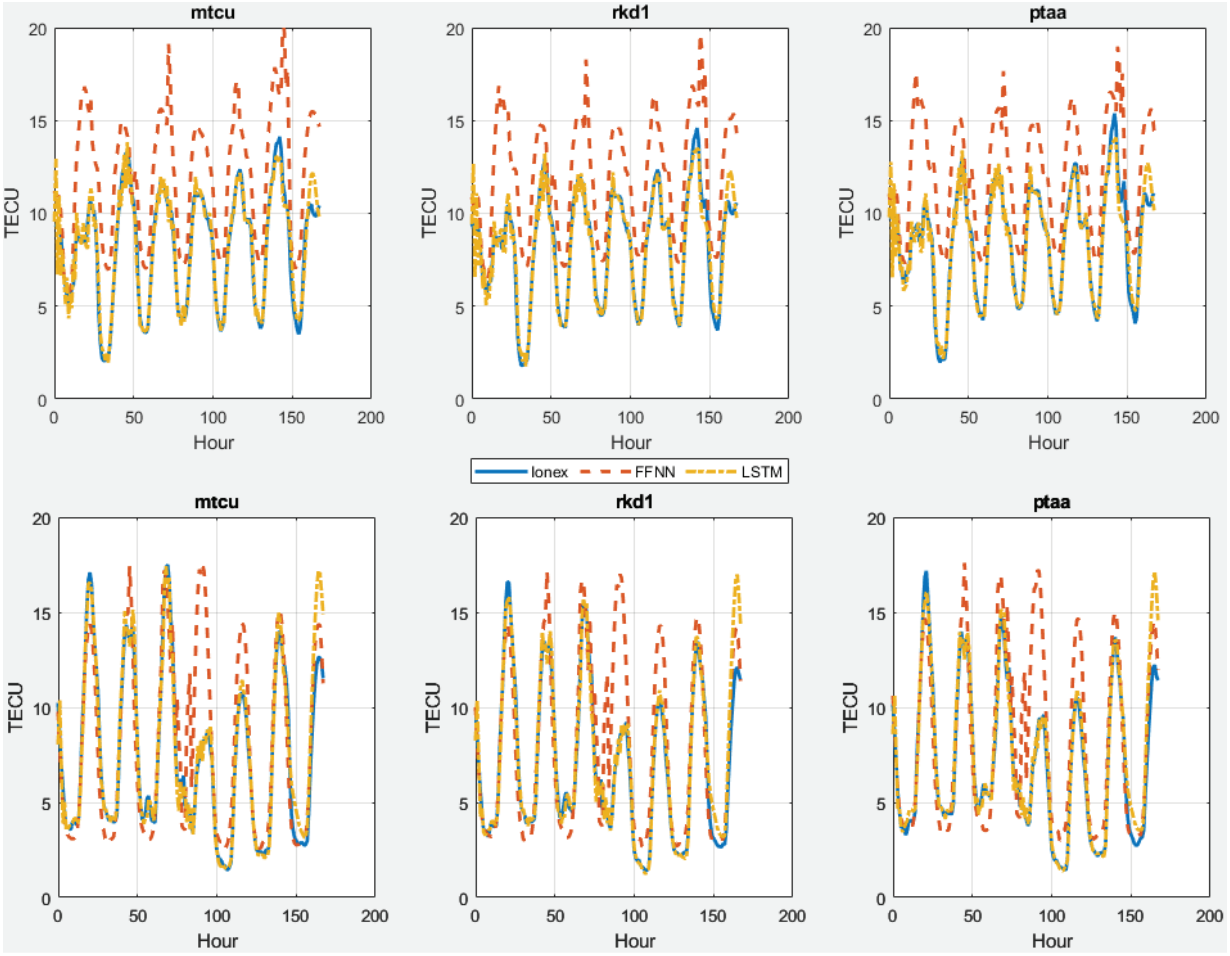

FIGURE 16 One-week comparisons (May 12–18 and October 9–15) between predictions made by Ionex, FFNN, and LSTM models

model can identify variations in the rapid products. By contrast, the FFNN model shows some difficulties in processing the data from May 2021. The FFN model was generally good for predictions using the October 2021 data except for the fourth day of prediction, which had relatively large errors. The same behaviors were observed on the right side of Figure 15. Table 6 compiles the statistical results from the processing and verifies that the proposed LSTM model outperforms the traditional FFNN model.

TABLE 6
One-Week VTEC Prediction RMSE in TECU

Period	Station	FFNN	LSTM
May 12–18	mtcu	4.17	0.75
	rkd1	4.02	0.72
	ptaa	3.86	0.74
October 9–15	mtcu	2.60	1.02
	rkd1	2.53	1.02
	ptaa	2.60	1.02

4 | EVALUATION OF PROPOSED IONOSPHERE MODEL IN SINGLE-FREQUENCY STANDARD POINT POSITIONING (SPP)

In this section, the performance of the proposed ionosphere model will be evaluated by applying it to a single-frequency SPP. A comparison will be presented between the rapid products, machine learning prediction products, and the IGS RT-GIM. The functional model for single-frequency SPP is shown in Equation (13) as follows.

$$P^j = \rho^j + dt_r - dT^j + m^j T + I^j + b_P - B_P^j \tag{13}$$

where j represents the satellite index, P is the pseudorange in meters, ρ is the geometric range, dt_r is receiver clock in meters, dT^j is satellite j clock, $m^j T$ is slant troposphere delay, I^j is satellite j ionosphere delay on the first frequency, b_P is receiver clock bias for the pseudorange, and B_{P}^j is satellite j clock bias for the pseudorange.

The receiver clock bias can be absorbed by the receiver clock; orbit error, clock error, receiver clock error, troposphere, ionosphere, and satellite bias need to be solved. To evaluate the impact of ionosphere errors, and CNES, post-processed products are used to compensate for orbit error, clock error, and satellite bias. Applying different ionosphere products used to mitigate ionosphere error will permit us to determine the impact of the accuracy of the ionosphere on the code-based positioning results. The troposphere, receiver clock, and position are the only parameters that will need to be estimated from the filter.

The ionosphere products are generated as vertical TECU. Equation (14) can be applied to obtain the slant ionosphere delays in meters.

$$I_{vtec}^j = \frac{40.3 \times 10^{16}}{f^2} I_{TECU} \tag{14}$$

$$I^j = m_I^j I_{vtec}^j$$

where I_{TECU} is the vertical ionosphere in TECU, I_{vtec}^j is the vertical delay in meters, and m_I^j is the ionosphere mapping function of satellite j. Both the vertical ionosphere delays are at the ionosphere pierce point (IPP). The vertical delay is based on rotated TEC maps and the four-point formula (Schaer & Gurtner, 1998).

As the test region covers an extensive area of northwestern continental U.S. and part of western Canada, three stations within this area from the NGS CORS network were selected to verify the predicted ionosphere performance. The stations selected are located along the U.S.-Canada border, including, mtcu in Montana

TABLE 7
May 12, 2021: Single-Frequency Positioning RMSE in Meters

Station	Rapid Ionosphere	ML Predicted Ionosphere	IGS RT-GIM
mtcu	0.743	0.805	0.938
ptaa	0.854	0.842	0.984
rkd1	0.846	0.883	1.014

TABLE 8
October 9, 2021: Single-Frequency Positioning RMSE in Meters

Station	Rapid Ionosphere	ML Predicted Ionosphere	IGS RT-GIM
mtcu	0.664	0.665	0.696
ptaa	0.946	0.941	0.927
rkd1	0.857	0.871	0.859

and rkd1 and ptaa in Washington. To verify the quality of the predicted ionosphere compared to that generated based on rapid products from IGS, both dual-frequency float PPP and single-frequency accuracy were analyzed. Only GPS and GLONASS systems were used in the analysis. The predicted ionosphere products were used in uncombined PPP processing.

The rapid ionosphere from CODE, the machine learning predicted ionosphere, and the IGS-RT-GIM in spherical harmonics were used to run the single-frequency positioning engine. The 24-hour dual-frequency PPP results were used as references to compute the position RMSE. The position RMSEs for the three stations and 24 hours are shown in Table 7 and Table 8. Table 7 shows the results from the May 12, 2021 dataset which was considered an ionosphere-active day. As shown in Table 7, when the ionosphere is active, the position accuracy from machine learning is very close to that of the rapid products; the accuracy from IGS-RT-GIM is somewhat worse than the other two when tested under these conditions. By contrast, Table 8 shows the ionosphere on a quiet day. Under these conditions, there were no obvious differences between the three types of ionosphere products.

5 | CONCLUSION

In this paper, we propose an LSTM-based deep learning NN that provides real-time regional ionosphere predictions. Various deep-learning settings were tested. Our results indicate that a two-LSTM-layer setting with 400 and 200 hidden units, respectively, results in the best overall performance. The LSTM deep learning approach can achieve higher accuracy than the broadcast model. Our research revealed that, on quiet ionosphere days, a daily RMSE of 0.8 TECU was observed. This value is more accurate than the RMSE of 1.25 TECU generated by the broadcast model. On active ionosphere days, improvements from 1.88 to 1.66 TECU were achieved. Thus, we can conclude that the proposed ionosphere prediction approach outperforms the broadcast IGS products in environments with different geomagnetic activity strengths. Compared to the traditional methods currently in use at IGS processing centers, this method has a simpler structure as it does not require continuous data links for GNSS observations. Verification of our results revealed that the deep learning predicted ionosphere method provides displays similar performance to IGS rapid products and improved performance compared to IGS RT-GIMs; this method also outperforms traditional FFNN models.

Therefore, the use of this method may improve the accuracy of the rapid products for real-time applications. Future work will include NN training with additional critical information, including standard deviation values from rapid products.

ACKNOWLEDGMENTS

The financial support from the Natural Sciences and Engineering Research Council of Canada (NSERC) is greatly acknowledged. IGS, CODE, and CNES are gratefully acknowledged for providing correction products. We likewise appreciate NOAA CORS for providing GNSS observation data.

CONFLICT OF INTEREST

The authors declare no potential conflict of interest.

REFERENCES

Aggrey, J., & Bisnath, S. (2019). Improving GNSS PPP Convergence: The case of atmospheric-constrained, multi-GNSS PPP-AR. *Sensors*, 587. https://doi.org/10.3390/s19030587

Boulch, A., Cherrier, N., & Castaings, T. (2018). Ionospheric activity prediction using convolutional recurrent neural networks. *IEEE transactions on Big Data*. https://doi.org/10.48550/arXiv.1810.13273

Chung, J., Gulcehre, C., Cho, K., & Bengio, Y. (2014). Empirical Evaluation of Gated Recurrent Neural Networks on Sequence Modeling. *NIPS 2014 Deep Learning and Representation Learning Workshop*. https://doi.org/10.48550/arXiv:1412.3555

Fang, W., Jiang, J., Liu, S., Gong, Y., Tao, Y., Tang, Y., Yan, P., Luo, H., & Liu, J. (2020). A LSTM algorithm estimating pseudo measurements for aiding INS during GNSS signal outages. *Remote Sensing*, 256. https://doi.org/10.3390/rs12020256

Ferreira, A. A., Borges, R. A., Paparini, C., Ciraolo, L., & Radicella, S. M. (2017). Short-term estimation of GNSS TEC using a neural network model in Brazil. *Advances in Space Research*, 1765–1776. https://doi.org/10.1016/j.asr.2017.06.001

Habarulema, J. B., McKinnell, L.-A., & Opperman, D. L. (2011). Regional GPS TEC modeling; attempted spatial and temporal extrapolation of TEC using neural networks. *Journal of Geophysical Research*. https://doi.org/10.1029/2010JA016269

Han, Y., Wang, L., Fu, W., Zhou, H., Li, T., & Chen, R. (2022). Machine learning-based short-term GPS TEC forcasting during high solar activity and magnetic storm periods. *IEEE Journal of Selected Topics in Applied Earth Observations and Remote Sensing*, 115–126. https://doi.org/10.1109/JSTARS.2021.3132049

Haykin, S. (2009). *Neural Networks and Learning Machines. 3rd Edition.* Pearson.

Hochreiter, S., & Schmidhuber, J. (1997). Long short-term memory. *Neural Computation*, 1735–1780. https://doi.org/10.1162/neco.1997.9.8.1735

IGS: IGS State Space Representation (SSR) Format Version 1.00. (2020). Retrieved March 3, 2023, from https://files.igs.org/pub/data/format/igs_ssr_v1.pdf

Iluore, K., & Lu, J. (2022). Long short-term memory and gated recurrent neural networks to predict the ionospheric vertical total electron content. *Advances in Space Research*, 652–665. https://doi.org/10.1016/j.asr.2022.04.066

Karevan, Z., & Suykens, J. A. (2020). Transductive LSTM for time-series prediction: An application to weather forecasting. *Neural Networks*, 1–9. https://doi.org/10.1016/j.neunet.2019.12.030

Kaselimi, M., Doulamis, N., Doulamis, A., & Delikaraoglou, D. (2020). A sequence-to-sequence temporal convolutional neural network for ionosphere prediction using GNSS observations. *2020 XXIV ISPRS Congress*, 813–820. Nice, France. https://doi.org/10.5194/isprs-archives-XLIII-B3-2020-813-2020

Leandro, R. F., & Santos, M. C. (2007). A neural network approach for regional vertical total electron content modelling. *Studia Geophysica et Geodaetica*, 279–292. https://doi.org/10.1007/s11200-007-0015-6

Liu, L., Zou, S., Yao, Y., & Wang, Z. (2020). Forcasting global ionospheric TEC using deep learning Approach. *Space Weather*. https://doi.org/10.1029/2020SW002501

Liu, Q., Hernández-Pajares, M., Yang, H., Monte-Moreno, E., Roma-Dollase, D., García-Rigo, A., Li, Z., Wang, L., Laurichesse, D., Blot, A., Zhao, Q., Zhang, Q., Hauschild, A., Agrotis, L., Schmitz, M., Wübbena, G., Stürze, A., Krankowski, A., Schaer, S., Feltens, J., Komjathy, A., & Ghoddousi-Fard, R. (2021). The cooperative IGS RT-GIMs: a reliable estimation of the global ionospheric electron content distribution in real time. Earth System Science Data, 4567–4582. https://doi.org/10.5194/essd-13-4567-2021

Mallika, I. L., Ratnam, D., Ostuka, Y., & Sivavaraprasad, G. (2019). Implementation of hybrid ionospheric TEC forecasting algorithm using PCA-NN method. *IEEE Journal of Selected Topics in Applied Earth Observation and Remote Sensing*, 371–281. https://doi.org/10.1109/JSTARS.2018.2877445

Mallika, L., Ratnam, D. V., Raman, S., & Sivavaraprasad, G. (2020). Machine learning algorithm to forecast ionospheric time delays using global navigation satellite system observations. *Acta Astronautica*, 221–231. https://doi.org/10.1016/j.actaastro.2020.04.048

Mckinnell, L.-A., & Poole, W. V. (2004). Neural network-based ionospheric modelling over the South African region. *South African Journal of Science*. https://journals.co.za/doi/pdf/10.10520/EJC96195

Nie, Z., Yang, H., Zhou, P., Gao, Y., & Wang, Z. (2019). Quality assessment of CNES real-time ionospheric products. *GPS Solutions*. https://doi.org/10.1007/s10291-018-0802-2

Perez, R. O. (2018). Using tensorFlow-based neural network to estimate GNSS signal frequency ionospheric delay (IONONet). *Advances in Space Research*, 1607–1618. https://doi.org/10.1016/j.asr.2018.11.011

Products. (2020). Retrieved from INTERNATIONAL GNSS SERVICE: https://igs.org/products/

RTCM-SC: Proposal of new RTCM SSR messages, SSR Stage 2: Vertical TEC (VTEC) for RTCM Standard 10403.2 Differential GNSS Services - Version 3. (2014). RTCM Special Committee, 104.

Schaer, S. (1997). *How to use CODE's global ionosphere maps.* Astronomical Institute, University of Berne.

Schaer, S., & Gurtner, W. (1998). IONEX: The IONosphere Map EXchange. *Proc. of the IGS AC Workshop.* Darmstadt, Germany.

Sorkhabi, O. M. (2021). Deep learning of total electron content. *SN Appl. Sci.*, 685. https://doi.org/10.1007/s42452-021-04674-6

Sun, W., Xu, L., Huang, X., Zhang, W., Yuan, T., Chen, Z., & Yan, Y. (2017). Forecasting of ionospheric vertical total electron content (TEC) using LSTM networks. *Proc. of the 2017 International Conference on Machine Learning and Cybernetics*, 340–344. Ningbo, China. https://doi.org/10.1109/ICMLC.2017.8108945

Tang, R., Zeng, F., Chen, Z., Wang, J.-S., Huang, C.-M., & Wu, Z. (2020). The comparison of predicting storm-time ionospheric TEC by three methods: ARIMA, LSTM, and Seq2Seq. *Atmosphere*. https://doi.org/10.3390/atmos11040316

Ulukavak, M. (2021). Deep learning for ionospheric TEC forcasting at mid-latitude stations in Turkey. *Acta Geophysica*, 589–606.

Uwamahoro, J. C., Giday, N. M., Habarulema, J. B., Katamzi-Joseph, Z. T., & Seemala, G. K. (2018). Reconstruction of storm-time total electron content using ionospheric tomography and artificial neural networks: A comparative study over the African Region. *Radio Science*, 1328–1345. https://doi.org/10.1029/2017RS006499

Xia, G., Zhang, F., Wang, C., & Zhou, C. (2021). ED-ConvLSTM: A novel global ionospheric total electron content medium-term forcast model. *Space Weather*. https://doi.org/10.1029/2021SW002959

Xiang, Y. (2018). *Carrier Phase-Based Ionospheric Modeling and Augmentation in Uncombined Precise Point Positioning.* Calgary: University of Calgary Thesis.

Xiong, P., Zhai, D., Long, C., Zhou, H., Zhang, X., & Shen, X. (2021). Long short-term memory neural network for ionospheric total electron content forcasting over China. *Space Weather*. https://doi.org/10.1029/2020SW002706

Zhang, Q., & Zhao, Q. (2019). Analysis of the data processing strategies of spherical harmonic expansion model on global ionosphere mapping for moderate solar activity. *Advances in Space Research*, 1214–1226. https://doi.org/10.1016/j.asr.2018.10.031

How to cite this article: Chen, J., & Gao, Y. (2023). Real-time ionosphere prediction based on IGS rapid products using long short-term memory deep learning. *NAVIGATION, 70*(2). https://doi.org/10.33012/navi.581